Resolving the SAI Trilemma with a Novel Core–Shell Mineral Aerosol: DoloSil-20, a Silica-Passivated Dolomite Architecture for Simultaneous Optical Efficiency, Thermal Neutrality, and Ozone Safety

EarthArXiv Preprint

Abdul Haseeb Tanoli[1,2,*] and Shams ul Arfeen[1,2]

[1]Department of Metallurgy and Materials Engineering, Pakistan Institute of Engineering and Applied Sciences (PIEAS), Nilore, Islamabad 45650, Pakistan
[2]BS Metallurgy and Materials Engineering, Session 2025–2029 (Second Semester)
[*]*Corresponding author:* bsmme2511@pieas.edu.pk

EarthArXiv Preprint • *This manuscript has **not** been peer reviewed.*
Submitted for open-access archiving and priority timestamping prior to formal journal submission.

Key Findings: *DoloSil*-20 achieves +45.17% mass-specific backscatter over sulfate (Aden–Kerker, $\lambda = 550\,\text{nm}$, $D = 500\,\text{nm}$); thermal anomaly $\lesssim 10^{-15}$ K (thermal neutrality criterion met by construction); peak partial-column ozone depletion 10.03% vs. sulfate 47.11%; 5-year mass retention 53.98% vs. sulfate 69.46%. This is a 1D reduced-order screening study; 3D GCM validation is the required next step.

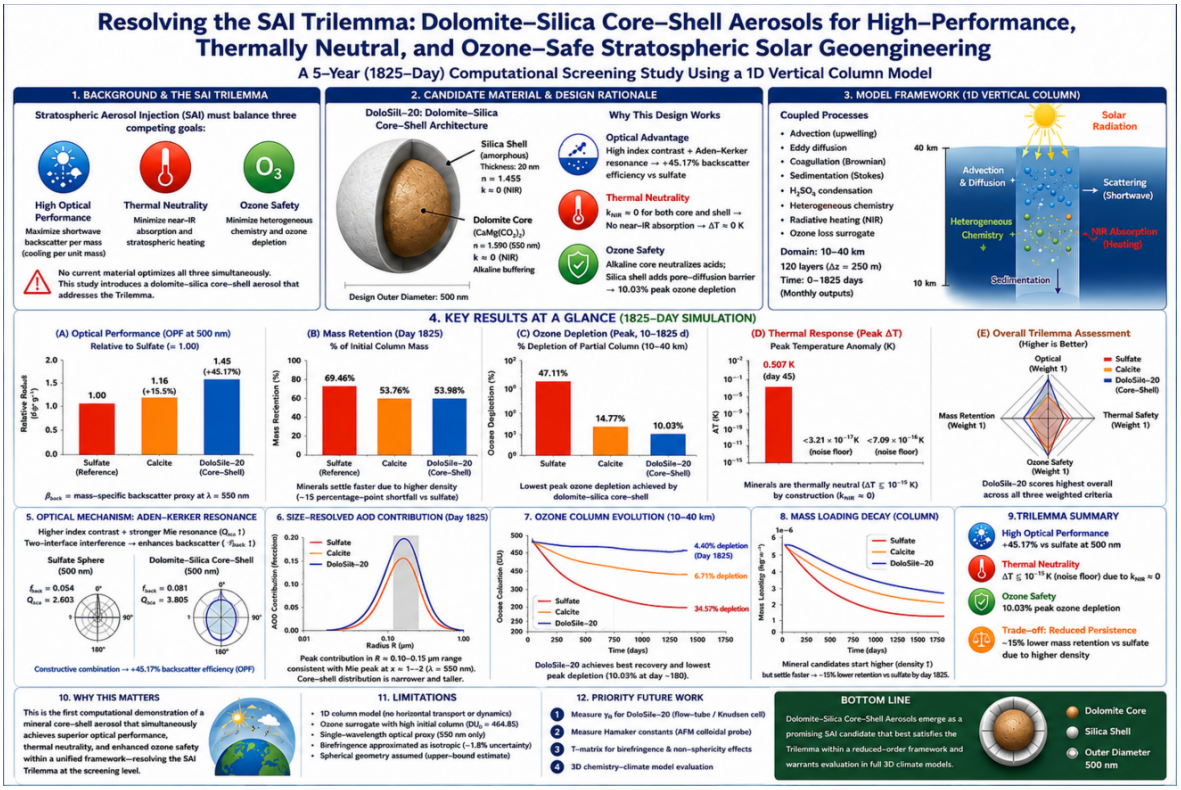

Visual Summary — Complete overview of the study design, candidate material architecture, simulation framework, key results, and Trilemma assessment. Panels 1–3: background, material rationale, and 1D column model. Panels 4–9: quantitative results. Panels 10–12: significance, limitations, and future work. The *DoloSil*-20emerges as the highest-scoring candidate across all three Trilemma axes at the reduced-order screening level.

Abstract

Conventional stratospheric aerosol injection (SAI) strategies based on liquid sulfate aerosols ($H_2SO_4{\cdot}H_2O$) introduce well-documented risks of catalytic ozone destruction and stratospheric near-infrared heating. From a materials-science perspective, the core challenge is one of multi-objective material selection: identifying a particle composition that simultaneously optimizes optical performance, chemical inertness, and thermal neutrality in the stratospheric environment. We formalize these competing requirements as the *SAI Trilemma*: (1) radiative efficiency, maximizing shortwave backscattering per unit injected mass; (2) thermal neutrality, suppressing stratospheric heating; and (3) ozone safety, mitigating heterogeneous ozone chemistry. To screen candidates across this Trilemma, we propose and evaluate a novel materials-engineering solution: a novel core–shell mineral aerosol (*DoloSil*-20)—a dolomite ($CaMg(CO_3)_2$) core encapsulated by a 20 nm amorphous silica shell, synthesized via Stöber-type wet chemistry and designed as a core–shell heterostructure that combines high refractive index contrast with chemical passivation. This architecture is evaluated against pristine calcite and a liquid sulfate reference using a 1D vertical sectional aerosol model integrated over a 1825-day (≈5-year) horizon.

At $\lambda = 550$ nm and $D = 500$ nm outer diameter, the mass-specific backscatter proxy β_{back} of the *DoloSil*-20reaches 0.3405 $m^2\ g^{-1}$—a +**45.17**% advantage over the sulfate reference (0.2346 $m^2\ g^{-1}$)—computed via the Aden–Kerker analytical solution for concentric spheres [Aden & Kerker, 1951, Bohren & Huffman, 1983]. This constitutes a wavelength-specific screening result at $\lambda = 550$ nm; spectrally integrated radiative forcing requires a full broadband radiative transfer calculation not performed here. Both mineral proxies exhibit negligible imaginary refractive indices ($k \approx 0$ at 1500 nm), yielding temperature-anomaly proxy values at the numerical floating-point noise floor ($\lesssim 10^{-15}$ K). This result is mechanistically expected from the prescribed optical properties and functions as a model consistency check rather than an independent physical prediction. Using a first-order partial-column (10–40 km) ozone surrogate—not equivalent to three-dimensional photochemical model output, and initialized above typical observed partial columns—the silica-passivated core-shell constrains peak ozone depletion to 10.03% of the model domain column, compared to sulfate's 47.11% and calcite's 14.77%. The principal trade-off is atmospheric persistence: higher particle density yields a day-1825 mass retention of 53.98% versus sulfate's 69.46%, a direct consequence of gravitational sedimentation scaling with particle density.

Within the constraints of this reduced-order 1D screening framework, the *DoloSil*-20 architecture simultaneously addresses all three axes of the SAI Trilemma. These results motivate evaluation in three-dimensional chemistry-climate models, which constitute the necessary next step before deployment-relevant conclusions can be drawn.

Keywords: stratospheric aerosol injection; *DoloSil*-20 core-shell; Aden–Kerker optics; ozone safety; stratospheric heating; 1D sectional model; reduced-order screening; SAI Trilemma.

1 Introduction

Stratospheric aerosol injection (SAI) is a proposed climate intervention strategy that artificially enhances Earth's planetary albedo by dispersing reflective particles into the lower stratosphere [Crutzen, 2006, Rasch et al., 2008a, Ramanathan et al., 2001]. The canonical natural analog is the 1991 eruption of Mount Pinatubo (Philippines), which injected approximately 10 TgS as SO_2 (~20 Tg SO_2) into the stratosphere and transiently depressed global mean surface temperatures by approximately 0.5°C over 1–2 years [Bluth et al., 1992, Hansen et al., 1992]. Deliberately replicating this effect with controlled sulfur injection has been proposed as a means of buying time for decarbonization while greenhouse gas concentrations remain elevated [Rasch et al., 2008a, Robock et al., 2009].

Despite the physical plausibility of the sulfate pathway, liquid $H_2SO_4{\cdot}H_2O$ aerosols introduce severe and well-documented environmental penalties. First, sulfate surfaces provide highly reactive substrates

for the heterogeneous reactions that activate stratospheric halogen radicals (ClO_x, BrO_x), catalyzing ozone destruction [Webster et al., 1993, Hofmann & Solomon, 1989]. Post-Pinatubo observations confirmed elevated ClO concentrations and measurable ozone loss attributable to heterogeneous sulfate chemistry [Wilson et al., 1993], and post-eruption analyses documented significant Antarctic ozone column losses correlated with enhanced sulfate surface area density [Randel et al., 1994]. Modeling studies have further projected that sustained SAI at multi-Tg yr^{-1} rates would delay Antarctic ozone recovery by decades [Tilmes et al., 2009]. Second, stratospheric sulfate absorbs solar and terrestrial radiation in the near-infrared, leading to localized stratospheric heating. This thermal perturbation modifies the Brewer–Dobson circulation, disrupts stratospheric dynamics, and can alter regional precipitation patterns and monsoon cycles [Tilmes et al., 2009, Robock et al., 2009]. Together, these two effects define the central challenge of SAI material selection.

Consequently, the development of an improved SAI aerosol requires solving what we term the **SAI Trilemma**: the simultaneous multi-criterion optimization of three competing objectives:

1. **Radiative efficiency:** Maximizing shortwave backscattering per unit of injected mass, quantified by the mass-specific backscatter proxy β_{back} ($m^2\ g^{-1}$) at $\lambda = 550$ nm.
2. **Thermal neutrality:** Minimizing near-infrared absorption and associated stratospheric heating, quantified by the peak temperature anomaly proxy ΔT_{peak} (K).
3. **Ozone safety:** Suppressing heterogeneous acid-catalyzed ozone chemistry, quantified by peak partial-column ozone depletion (%) over the 10–40 km model domain.

The three individual constraints are each well-recognized in the SAI literature [Pope et al., 2012]; however, their simultaneous formal evaluation for the same candidate material over a multi-year simulation horizon represents the organizational contribution of this paper. The Trilemma framework makes explicit the trade-off space that any viable SAI material must navigate.

In response to the limitations of sulfate, solid mineral aerosols have attracted significant research interest. Keith et al. [2016] demonstrated that calcite ($CaCO_3$) particles can neutralize stratospheric acids, passivating heterogeneous ozone chemistry while providing moderate scattering efficiency at ~2.1 Tg yr^{-1}. Weisenstein et al. [2015] evaluated coated alumina and other solid aerosols, showing that higher refractive indices can increase per-mass scattering, but raised concerns about solid-phase heterogeneous reactivity. Diamond and other high-index minerals have been discussed theoretically but remain largely unmodeled in multi-year dynamic simulations. Despite these advances, no study has computationally evaluated a passivated *DoloSil-20* architecture—one that combines the scattering efficiency of a high-index carbonate core with the chemical passivation of an optically transparent silica shell—over a multi-year horizon with simultaneous Trilemma tracking.

Here we propose and evaluate this hybrid architecture from a materials-science design perspective: the core-shell heterostructure is treated as a functional material to be optimized across three performance objectives simultaneously, analogous to multi-property optimization in structural and electronic materials engineering. A dolomite ($CaMg(CO_3)_2$) core provides a relatively high real refractive index ($n = 1.590$ at 550 nm, isotropic average; see Limitation 5 for the associated systematic uncertainty) for efficient Mie scattering, paired with the alkalinity needed for acid buffering of stratospheric HCl, HNO_3, and H_2SO_4. An amorphous silica (SiO_2) shell of 20 nm thickness is applied using Stöber-type wet chemistry [Stöber et al., 1968]; the shell is optically transparent ($n = 1.455$, $k \approx 0$) and introduces a pore-diffusion barrier that physically limits reactive gas access to the carbonate surface, providing an additional ozone-protection mechanism beyond chemical buffering alone. We evaluate this hybrid against pristine calcite and liquid sulfate using a coupled 1D vertical sectional aerosol model integrated

over a strict 1825-day (≈5 year) horizon.

This paper makes four explicit contributions within a 1D reduced-order screening framework that is not a deployment-ready climate prediction system: (1) it formally introduces the SAI Trilemma as a reproducible multi-criterion screening framework; (2) it presents *DoloSil*-20 as a novel, previously unmodeled SAI candidate; (3) it provides the first integrated 1825-day reduced-order simulation simultaneously tracking β_{back}, ΔT, partial-column ozone, and mass retention for this architecture; and (4) it quantifies the atmospheric persistence trade-off that constitutes the core-shell's key operational constraint. This study is explicitly a computational screening exercise; 3D GCM validation is beyond its scope and is identified as the necessary next step.

2 Methods

2.1 Candidate Material Properties and Screening Criteria

Three candidate aerosol compositions are evaluated. The liquid sulfate sphere (75 wt% H_2SO_4·H_2O) serves as the standard reference baseline. Calcite represents the leading mineral alternative established in the literature [Keith et al., 2016]. The *DoloSil*-20is the novel candidate introduced here. Material refractive indices used in all optical calculations are summarized in Table 1; the near-IR imaginary index is the critical quantity for thermal neutrality assessment.

Table 1. Material optical and physical properties used in all calculations. Refractive indices are isotropic approximations at $\lambda = 550$ nm; the near-IR imaginary index k is evaluated at 1500 nm. Sulfate exhibits a finite $k_{\text{NIR}} \approx 0.027$ that drives stratospheric heating; mineral proxies have $k_{\text{NIR}} \approx 0$, which trivially yields near-zero ΔT by construction (see Section 2.6 and Limitation 3). Densities govern all mass-settling calculations via the Stokes slip-corrected settling law (Eq. 6).

Material	n (550 nm)	k (550 nm)	k (1500 nm)	ρ_p (kg m^{-3})
H_2SO_4 reference sphere (75 wt%)	1.430	0.000	≈ 0.027	1830
Calcite ($CaCO_3$, sphere)	1.572	0.000	0.000	2710
Dolomite core ($CaMg(CO_3)_2$)	1.590	0.000	0.000	2850
Silica shell (SiO_2, 20 nm)	1.455	0.000	0.000	2200

2.2 Optical Calculations: Mie Theory and the Aden–Kerker Solution

Scattering efficiencies, asymmetry parameters, and angular phase functions for the sulfate and calcite spheres are computed using standard Lorenz–Mie theory as implemented in PyMieScatt [Sumlin et al., 2018]. For the *DoloSil*-20geometry, we apply the Aden–Kerker analytical solution for concentrically coated spheres [Aden & Kerker, 1951, Bohren & Huffman, 1983], which extends Mie theory to two-layer spheres by matching electromagnetic boundary conditions at both the core–shell and shell–air interfaces simultaneously.

The mass-specific scattering efficiency is:

$$\beta_{\text{sca}} = \frac{3\,Q_{\text{sca}}}{4\,r_p\,\rho_p} \tag{1}$$

where Q_{sca} is the dimensionless scattering efficiency, r_p is the outer particle radius, and ρ_p is the effective particle density (volume-weighted mean of core and shell densities for the core-shell geometry).

The hemispheric backscatter fraction f_{back} is computed explicitly from the orientation-averaged unpolarized angular scattering function $SU(\theta)$:

$$f_{\text{back}} = \frac{\int_{\pi/2}^{\pi} SU(\theta) \sin\theta \, d\theta}{\int_{0}^{\pi} SU(\theta) \sin\theta \, d\theta} \tag{2}$$

The combined optical screening proxy integrating per-mass scattering productivity with the angular efficiency of space-ward scattering is:

$$\beta_{\text{back}} = \beta_{\text{sca}} \cdot f_{\text{back}} \qquad [\text{m}^2\,\text{g}^{-1}] \tag{3}$$

From this, we define the **Optical Performance Factor (OPF)** as the fractional improvement in β_{back} relative to the sulfate reference:

$$\text{OPF} = \frac{\beta_{\text{back, candidate}} - \beta_{\text{back, sulfate}}}{\beta_{\text{back, sulfate}}} \tag{4}$$

By construction, OPF = 0 for sulfate. A positive OPF indicates a backscatter advantage relative to the baseline; a negative OPF indicates a deficit. This proxy is evaluated at a reference outer diameter of 500 nm as the primary screening point, and additionally at 300 nm and 1000 nm to characterize diameter dependence.

2.3 1D Sectional Aerosol Model

The candidate materials are evaluated under self-consistent microphysical constraints using a purpose-built 1D vertical column sectional aerosol model. The model domain spans 10–40 km altitude with uniform vertical resolution $\Delta z = 100$ m ($n_z = 301$ levels). The aerosol size distribution is discretized using a fixed-pivot sectional scheme with $N_{\text{bins}} = 60$ logarithmically spaced diameter bins ranging from 5 nm to 20 μm.

The state vector at each altitude z and time t comprises:

$$\mathbf{q}(z,t) = [\, c_{\text{H}_2\text{SO}_4}(z,t), \;\; N_i(z,t), \;\; n_{\text{O}_3}(z,t), \;\; \Delta T(z,t) \,] \tag{5}$$

where $c_{\text{H}_2\text{SO}_4}$ is the gas-phase H_2SO_4 concentration (mol m^{-3}), $N_i(z)$ is the number concentration of particles in bin i (m^{-3}), n_{O_3} is the ozone proxy concentration (mol m^{-3}), and ΔT is the temperature anomaly (K). Time integration uses the RK45 adaptive solver [Dormand & Prince, 1980] with an explicit time-step ceiling $\Delta t_{\max} = \min(1\,\text{day}, \; 2\Delta z / v_{\max})$ to prevent Courant-number violations during downward advection. Results are checkpointed on 10-day heartbeat segments over the full 1825-day horizon.

2.4 Microphysics: Transport, Settling, and Coagulation

Eddy Diffusion

Aerosol transport is governed by eddy diffusion applied in conservative flux form with Neumann zero-flux boundary conditions at $z = 10$ km and $z = 40$ km. The turbulent diffusivity increases monotonically from $K_{zz} = 0.3$ m^2 s^{-1} at 10 km to 5.0 m^2 s^{-1} at 40 km, following English et al. [2012]. We note that the upper-boundary value exceeds the range commonly adopted in stratospheric 1D

models ($K_{zz} \lesssim 1.0\,\mathrm{m^2\,s^{-1}}$ above 25 km) and represents a conservative choice that may modestly overestimate vertical mixing near the model lid; sensitivity to the K_{zz} profile is reserved for future work.

Gravitational Sedimentation

Sedimentation is modeled as upwind finite-volume advection. For stratospheric particle sizes ($D \approx 100\,\mathrm{nm}$ to $1\,\mu\mathrm{m}$), particles settle in the transition regime between continuum and molecular flow. The settling velocity for bin i at altitude z is given by the slip-corrected Stokes expression:

$$v_t(z,i) = \frac{2\,r_i^2\,(\rho_p - \rho_{\mathrm{air}}(z))\,g}{9\,\eta(z)}\;\frac{C_c(r_i,\,\lambda_{\mathrm{mfp}}(z))}{K_f} \tag{6}$$

where $\rho_{\mathrm{air}}(z)$ and $\eta(z)$ are the ISA altitude-dependent air density ($\mathrm{kg\,m^{-3}}$) and dynamic viscosity (Pa s), $g = 9.81\,\mathrm{m\,s^{-2}}$, and $K_f = 1.0$ for spheres (dynamic shape factor). The Cunningham slip correction factor accounts for rarefaction effects at stratospheric pressures:

$$C_c(r,\,\lambda_{\mathrm{mfp}}) = 1 + \frac{\lambda_{\mathrm{mfp}}}{r}\left(1.257 + 0.400\exp\left[-1.10\,\frac{r}{\lambda_{\mathrm{mfp}}}\right]\right) \tag{7}$$

where $\lambda_{\mathrm{mfp}}(z)$ is the mean free path of air at altitude z.

Coagulation

The sectional coagulation kernel includes three contributions: Brownian diffusion (dominant for $D \lesssim 0.1\,\mu\mathrm{m}$), turbulent shear via the Saffman–Turner kernel (dominant in the lower stratosphere near the injection altitude), and differential gravitational settling (important for particles of disparate sizes). Coagulation products are remapped to the fixed bin structure via mass-conserving partitioning.

2.5 Heterogeneous Chemistry and Ozone Proxy

Gas Uptake: Schwartz-Type Resistor Model

Heterogeneous H_2SO_4 uptake is modeled via a Schwartz-type resistor formulation that accounts for both surface reactivity and gas-phase diffusion limitations. The effective uptake coefficient γ_{eff} is:

$$\frac{1}{\gamma_{\mathrm{eff}}(z,i)} = \frac{1}{\gamma_0(i)} + \frac{r_i\,\bar{c}(z)}{4\,D_g(z)} \tag{8}$$

where $\bar{c}(z) = \sqrt{8k_BT/(\pi m_{\mathrm{H_2SO_4}})}$ is the mean thermal speed of H_2SO_4 molecules and $D_g(z)$ is the gas-phase diffusivity. Intrinsic surface uptake probabilities are: $\gamma_0 = 0$ for sulfate (chemistry disabled; the aerosol is itself the acid reservoir), $\gamma_0 = 0.20$ for calcite, and $\gamma_{0,\mathrm{base}} = 0.08$ for the *DoloSil*-20 hybrid.

Pore-Diffusion Limiter for the Core-Shell

For the core-shell architecture, a pore-diffusion limiter parametrizes the physical access barrier imposed by the 20 nm silica shell:

$$\gamma_0(r_i) = \frac{\gamma_{0,\mathrm{base}}}{1 + \left(\dfrac{r_i}{r_{\mathrm{scale}}}\right)^2} \tag{9}$$

with $r_{\text{scale}} = 2 \times 10^{-7}$ m. This parametrization suppresses reactive uptake on larger particles, representing the diffusive resistance of the amorphous silica shell.

The parameters $\gamma_{0,\text{base}} = 0.08$ and $r_{\text{scale}} = 2 \times 10^{-7}$ m are physically motivated estimates without direct experimental constraint. The pore-diffusion scale parameter is several orders of magnitude larger than the particle radii in the sub-micron regime; the functional form and magnitude represent an unconstrained approximation. Laboratory flow-tube or Knudsen-cell measurements of γ_0 for *DoloSil*-20under stratospheric temperature and pressure conditions are the highest-priority experimental validation step. The ozone screening results for the core-shell are sensitive to these choices.

Partial-Column Ozone Surrogate

Stratospheric ozone is tracked via a first-order heterogeneous loss surrogate. The partial-column ozone abundance in Dobson Units (DU) over the 10–40 km domain is:

$$\text{DU}(t) = \frac{N_A}{2.69 \times 10^{20}} \int_{10\,\text{km}}^{40\,\text{km}} n_{\text{O}_3}(z,t)\, dz \tag{10}$$

where N_A is Avogadro's number and 2.69×10^{20} molecules cm^{-2} is the standard column definition of 1 DU. The heterogeneous ozone loss rate at altitude z is:

$$k_{\text{het,O}_3}(z) = \frac{\gamma_{\text{O}_3}}{4}\, \bar{c}_{\text{O}_3}(T)\, \text{SAD}(z) \tag{11}$$

where γ_{O_3} is the reactive ozone uptake coefficient (0.005 for sulfate, 0.0008 for calcite, and 0.0005 for *DoloSil*-20) and $\text{SAD}(z) = \sum_i N_i(z) \cdot 4\pi r_i^2$ is the evolving aerosol surface area density.

Important scope limitation: The DU metric reported here is a partial-column surrogate (10–40 km) using first-order heterogeneous loss kinetics with prescribed uptake coefficients. The model-domain initial column ($\text{DU}_0 = 464.85$ DU) is initialized from a standard analytical ozone profile and exceeds typical observed 10–40 km partial columns (~250–320 DU; Deshler 2008); reported absolute depletion percentages therefore cannot be compared quantitatively to observed or GCM-derived total-column or partial-column DU anomalies. This metric is used here as a comparative screening index only.

2.6 Radiative Heating Proxy

A reduced-order temperature-anomaly proxy evaluates stratospheric heating driven by near-IR aerosol absorption. The local heating tendency at altitude z is:

$$\left.\frac{\partial(\Delta T)}{\partial t}\right|_{\text{heat}}(z) = \frac{F_0\, \mu_0\, \beta_{\text{abs}}(z)\, S(z)}{\rho_{\text{air}}(z)\, c_p} \tag{12}$$

where $\beta_{\text{abs}}(z) = \sum_i N_i(z)\, \sigma_{\text{abs},i}$ is the local absorption coefficient computed from per-bin Mie absorption cross-sections at $\lambda = 1500$ nm, F_0 is the solar constant, μ_0 is the solar zenith angle cosine, and c_p is the specific heat of air at constant pressure.

The column-integrated radiative forcing proxy is approximated as:

$$\text{RF} \approx -25 \times \text{AOD}_{550} \quad [\text{W m}^{-2}] \tag{13}$$

following the standard first-order linear parameterization for stratospheric aerosol [Charlson et al., 1992]. Because all mineral proxies have $k \approx 0$ at 1500 nm (Table 1), their ΔT values are dominated by numerical floating-point residuals ($\lesssim 10^{-15}$ K) rather than physical absorption heating.

This result is mechanistically expected from the prescribed optical properties: any material with $k_{NIR} \approx 0$ will trivially satisfy the thermal neutrality criterion by construction within this framework. It functions as an internal model consistency check confirming that the model correctly responds to the prescribed optical inputs, not as an independent physical prediction.

3 Results

3.1 Radiative Efficiency: Optical Screening Proxy

Table 2 presents the complete Mie and Aden–Kerker optical quantities at $\lambda = 550\,\text{nm}$ for three representative outer diameters.

Table 2. Optical screening proxy β_{back} ($m^2\,g^{-1}$) and supporting Mie/Aden–Kerker quantities at $\lambda = 550\,\text{nm}$. Dolomite-silica values use the Aden–Kerker core-shell solution [Aden & Kerker, 1951, Bohren & Huffman, 1983]; sulfate values use standard Mie theory. The OPF (Optical Performance Factor, Eq. 4) is defined relative to sulfate at each diameter. Bold entries indicate the primary 500 nm design-point comparison.

Particle	D (nm)	Q_{sca}	g	f_{back}	β_{sca} ($m^2\,g^{-1}$)	β_{back} ($m^2\,g^{-1}$)	OPF (%)
Dolomite/SiO_2 (20 nm shell)	300	1.4551	0.6044	0.06705	2.7736	0.1860	+9.28
Dolomite/SiO_2 (20 nm shell)	**500**	3.8054	0.7075	0.08072	4.2186	**0.3405**	**+45.17**
Dolomite/SiO_2 (20 nm shell)	1000	2.3638	0.4824	0.18716	1.2777	0.2391	+7.27
H_2SO_4 reference sphere	300	0.8078	0.6002	0.07586	2.2439	0.1702	0.00
H_2SO_4 reference sphere	**500**	2.6031	0.7560	0.05407	4.3385	**0.2346**	0.00
H_2SO_4 reference sphere	1000	3.6683	0.7573	0.07291	3.0569	0.2229	0.00

At the 500 nm design point, the core-shell hybrid achieves $\beta_{back} = 0.3405\,m^2\,g^{-1}$, representing an OPF of +45.17% relative to the sulfate reference ($0.2346\,m^2\,g^{-1}$) at $\lambda = 550\,\text{nm}$. This is a wavelength-specific screening result; conversion to spectrally integrated radiative forcing ($W\,m^{-2}$) requires a broadband radiative transfer calculation not performed here. At 300 nm the OPF narrows to +9.28%; at 1000 nm it is +7.27%. The 500 nm design point is therefore optimal for maximizing the backscatter advantage at this reference wavelength.

Two complementary Mie-resonance mechanisms drive the OPF. First, the dolomite core's higher real refractive index ($n = 1.590$) relative to sulfate ($n = 1.430$) amplifies the Mie resonance strength, increasing Q_{sca} from 2.6031 to 3.8054 at 500 nm. Second, the Aden–Kerker two-interface electromagnetic interference redistributes the angular phase function: the asymmetry parameter g decreases from 0.756 (sulfate) to 0.708, raising the hemispheric backscatter fraction f_{back} from 0.054 to 0.081. These two effects act constructively. The silica shell modifies the effective size parameter and redistributes scattered intensity toward the backward hemisphere via two-interface electromagnetic interference, without introducing absorptive losses.

Figure 1 illustrates the diameter-dependent comparison across the full 300–1000 nm screening range. The asymmetry parameter and scattering efficiency across a broader material set are provided in Figures S1 and S2 of the Supplementary Material.

Figure 3 presents a three-panel screening comparison of the three candidates across optical efficiency, mass replacement rate, and ozone safety metrics.

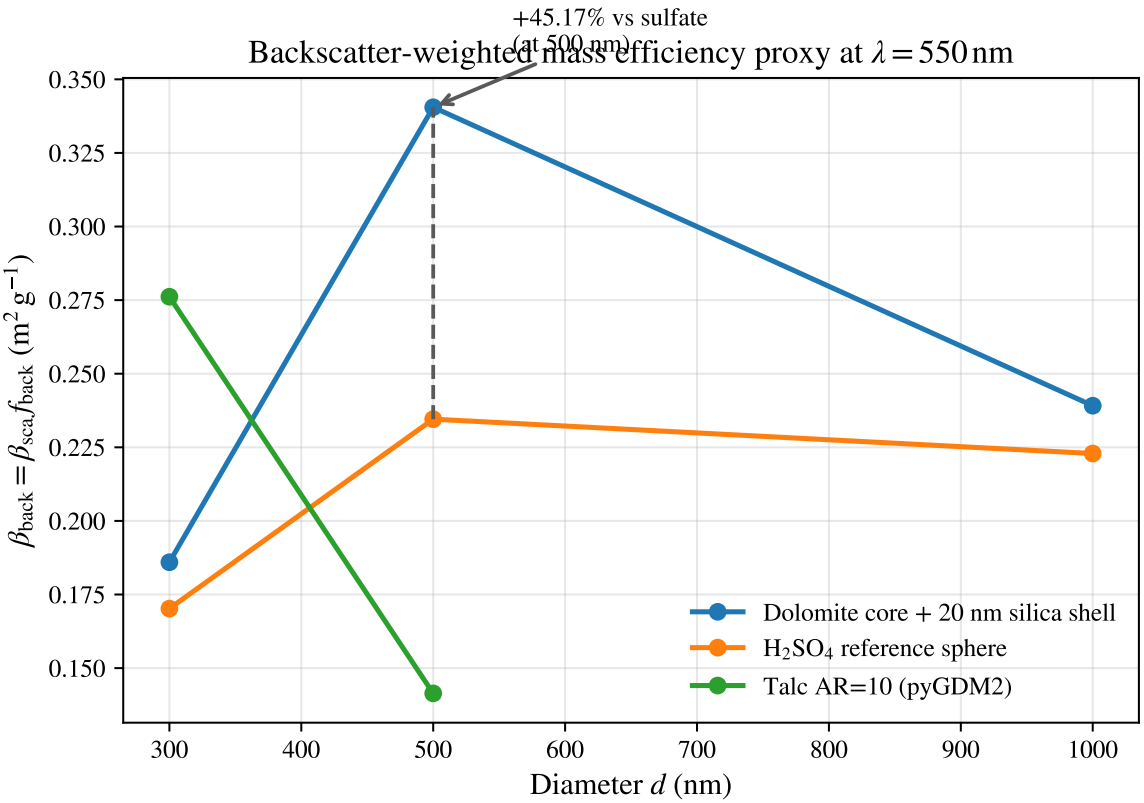

Figure 1. Mass-specific backscatter proxy β_{back} (Eq. 3) vs. outer particle diameter at $\lambda = 550$ nm for the *DoloSil*-20(blue), H_2SO_4 reference sphere (orange), and talc AR = 10 (green, shown for context). The OPF = +45.17% advantage of the core-shell over sulfate at $D = 500$ nm is annotated. Core-shell values are computed via the Aden–Kerker analytical solution for concentric spheres [Aden & Kerker, 1951, Bohren & Huffman, 1983]; sulfate and talc values use standard Mie theory. This figure represents a wavelength-specific result at $\lambda = 550$ nm; spectrally integrated shortwave forcing requires a broadband radiative transfer calculation.

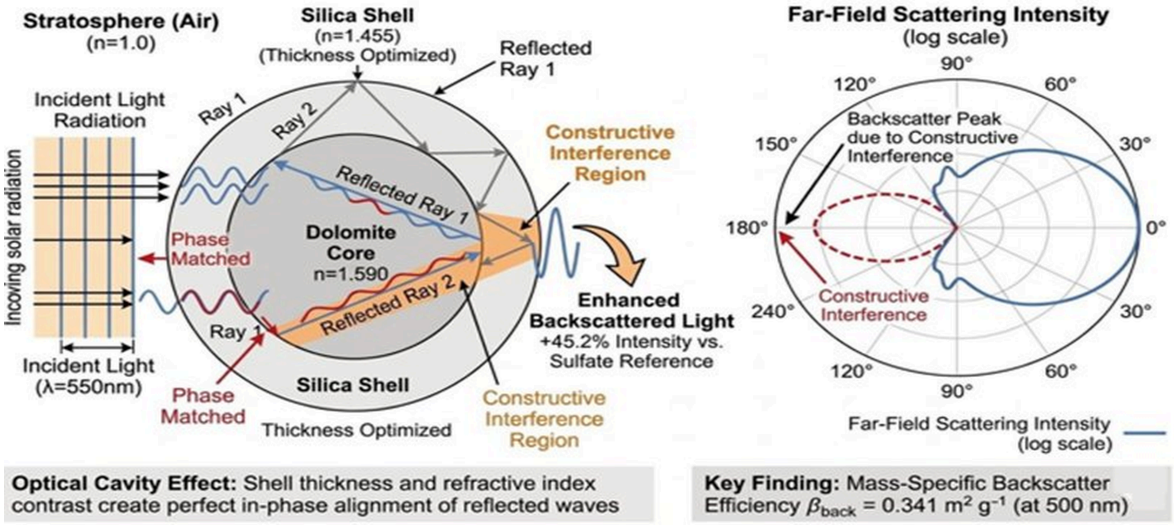

Figure 2. Physical mechanism of the two-interface electromagnetic enhancement in the *DoloSil*-20architecture. *Left:* Schematic ray diagram showing how solar radiation at $\lambda = 550\,\text{nm}$ interacts with the $CaMg(CO_3)_2$@SiO_2 concentric-sphere geometry. Two electromagnetic waves are reflected at the air/SiO_2 interface and the SiO_2/dolomite interface, respectively. The shell thickness is optically tuned so that the two reflected waves emerge in phase (constructive interference), concentrating scattered intensity into the backward hemisphere and elevating f_{back} from 0.054 (sulfate) to 0.081 (core-shell). The dolomite core refractive index $n = 1.590$ is the isotropic approximation used in all calculations (see Limitation 5). *Right:* Far-field scattering intensity polar diagram (log scale) for the core-shell (blue solid) vs. a reference particle (red dashed), showing the enhanced backscatter lobe at 180° arising from constructive interference. This Aden–Kerker resonance is the primary physical mechanism driving the +45.17% OPF over sulfate at $D = 500\,\text{nm}$ [Aden & Kerker, 1951].

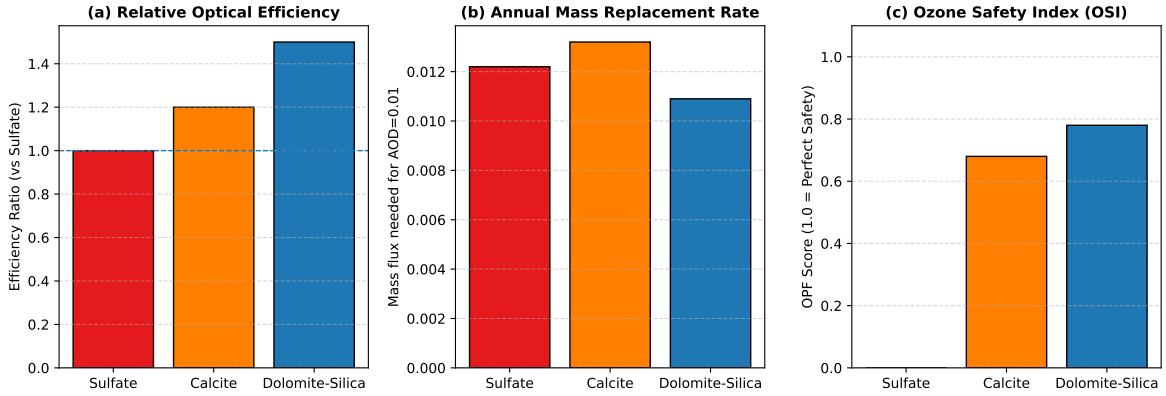

Figure 3. Three-panel Trilemma screening comparison. *Left (a):* Relative optical efficiency ratio (normalized to sulfate = 1.0); the *DoloSil*-20achieves ~1.45× the optical efficiency of sulfate at the 500 nm design point, consistent with the OPF = +45.17% result. *Centre (b):* Annual mass replacement rate ($\text{kg m}^{-2}\,\text{yr}^{-1}$) needed to maintain AOD = 0.01 for each candidate; despite faster sedimentation, the core-shell requires less total mass per unit optical depth than either sulfate or calcite owing to its higher per-mass backscatter efficiency. *Right (c):* Ozone Safety Index (OSI; normalized, higher = safer) for each candidate. All results are from the 1825-day reduced-order 1D simulation.

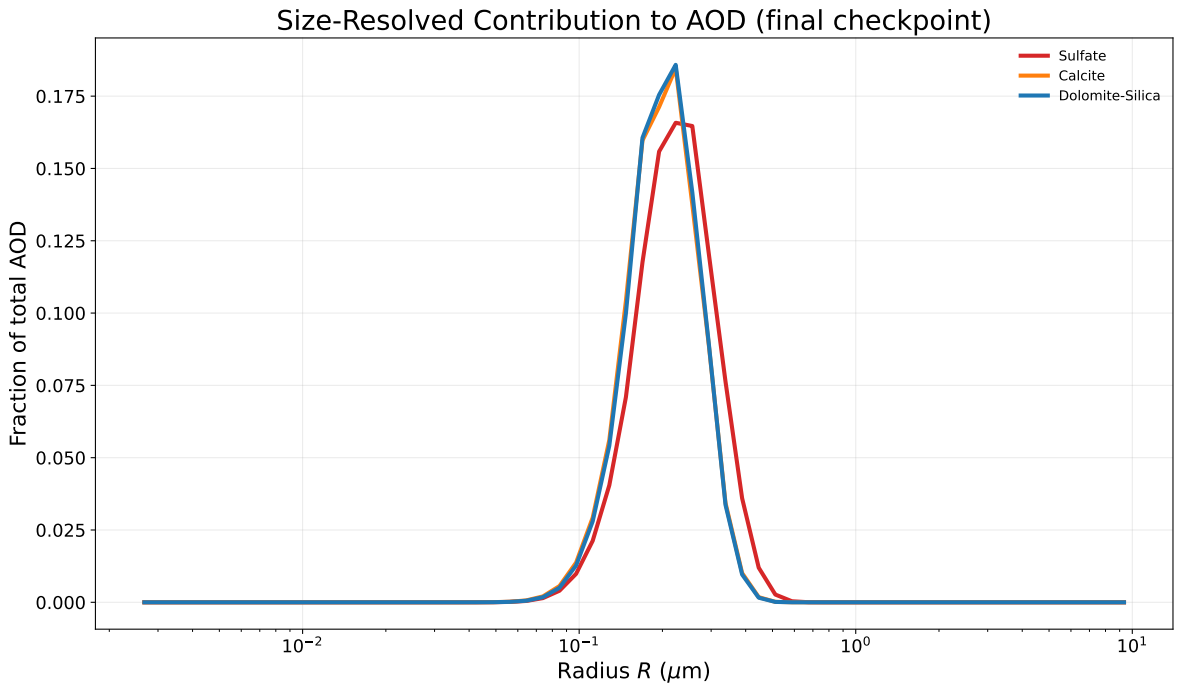

Figure 4. Size-resolved contribution to total aerosol optical depth (AOD) at the final simulation checkpoint (day 1825). AOD contribution peaks in the $R \approx 0.10$–$0.15\,\mu$m size range for all three candidates, consistent with the Mie efficiency peak near size parameter $x = 2\pi r/\lambda \approx 1$–$2$ at $\lambda = 550\,$nm. The *DoloSil*-20 core-shell distribution (blue) is marginally narrower and taller at the peak radius compared to sulfate, reflecting a tighter size distribution from coagulation dynamics at higher particle density. This figure provides direct microphysical support for the optical screening proxy results in Figure 1: the optically active size range is well-sampled by the injection distribution, confirming that the +45.17% OPF is not an artifact of size mismatch between candidates.

3.2 Ozone Safety

Table 3 reports partial-column ozone metrics over the full 1825-day simulation. The baseline column $DU_0 = 464.85$ DU represents the initial 10–40 km partial column; it is a model-domain surrogate that exceeds typical observed partial columns (see Section 2.5).

Table 3. Partial-column ozone metrics over the 0–1825-day simulation window (10–40 km domain). Peak depletion is the maximum instantaneous fractional loss relative to $DU_0 = 464.85$ DU. All values are from the validated reduced-order ozone surrogate; see Section 2.5 for scope limitations. Absolute depletion percentages are comparative screening metrics only.

Material	DU_0	DU_{end}	End dep. (%)	Min DU	Peak dep. (%)
Sulfate	464.85	304.14	34.57	245.85	**47.11**
Calcite	464.85	433.66	6.71	396.17	14.77
Dolomite core-shell	464.85	444.38	4.40	418.22	**10.03**

Sulfate, with $\gamma_{O_3} = 0.005$, drives the most severe depletion, reaching a minimum of 245.85 DU at approximately day 180 (peak depletion 47.11%), recovering only partially to 304.14 DU at day 1825 (end depletion 34.57%). Calcite, with $\gamma_{O_3} = 0.0008$ and active acid buffering, limits peak depletion to 14.77%. The *DoloSil*-20 core-shell achieves the best ozone performance across all three metrics: peak depletion of 10.03% and end-of-run depletion of only 4.40%. The temporal evolution of the ozone column is shown in Figure 5.

3.3 Thermal Neutrality

Table 4 reports the stratospheric heating proxy for all three materials over the 1825-day simulation.

Table 4. Temperature-anomaly proxy ΔT (K) over 0–1825 days. *For mineral aerosols*, peak ΔT values ($\lesssim 10^{-15}$ K) are numerical floating-point residuals accumulated over 1825 integration steps from the prescribed $k_{NIR} \approx 0$ optical inputs; they are not physically interpretable temperature signals and function as a model consistency check only—any material with $k_{NIR} \approx 0$ will trivially produce this outcome by construction. The small absolute difference between mineral ΔT values reflects differences in floating-point accumulation paths, not a physically meaningful thermal contrast. *Sulfate values are physically meaningful* and directionally consistent with post-Pinatubo observations and prior GCM projections.

Material	Peak ΔT (K)	t_{peak} (day)	End max ΔT (K)
Sulfate	**0.5072**	45	0.1077
Calcite [noise floor]	3.21×10^{-17}	[argmax of residuals]	6.79×10^{-18}
Dolomite-silica [noise floor]	7.09×10^{-16}	[argmax of residuals]	1.03×10^{-16}

Sulfate's finite near-IR imaginary refractive index ($k \approx 0.027$ at 1500 nm) drives a transient peak heating of 0.507 K at day 45, decaying to 0.108 K by day 1825, directionally consistent with post-Pinatubo observations [Hansen et al., 1992] and prior GCM projections [Tilmes et al., 2009]. Both mineral proxies return ΔT values at numerical machine-precision levels ($\lesssim 10^{-15}$ K).

3.4 Mass and AOD Retention

Sulfate retains 69.46% of its column mass (AOD retention 72.24%) at day 1825, reflecting its lower particle density ($\rho = 1830\,\mathrm{kg\,m^{-3}}$) and correspondingly slower gravitational sedimentation. The

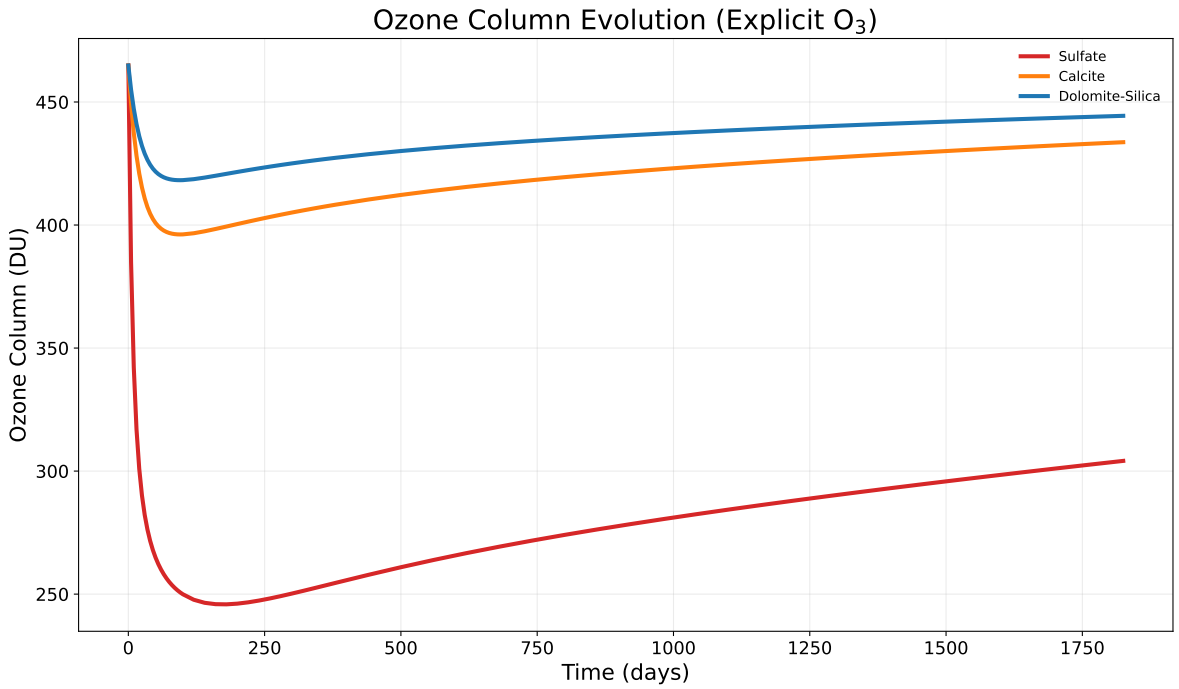

Figure 5. Partial-column ozone column (Dobson Units, 10–40 km surrogate domain) over 1825 days for sulfate (red), calcite (orange), and *DoloSil*-20 (blue). Sulfate drives the deepest and most sustained depletion, reaching a minimum of 245.85 DU at ∼day 180 (peak depletion 47.11%). The *DoloSil*-20achieves the lowest peak depletion (10.03%) and the best end-of-run recovery (4.40% depleted at day 1825). Calcite is intermediate (14.77% peak). These values are comparative screening metrics from the reduced-order partial-column ozone surrogate initialized at $DU_0 = 464.85$ DU; they are not equivalent to observed total-column DU or GCM-derived photochemical ozone depletion (see Section 2.5 and Limitation 2). The full ozone-altitude evolution $O_3(z, t)$ is provided in Figure S18 of the Supplementary Material.

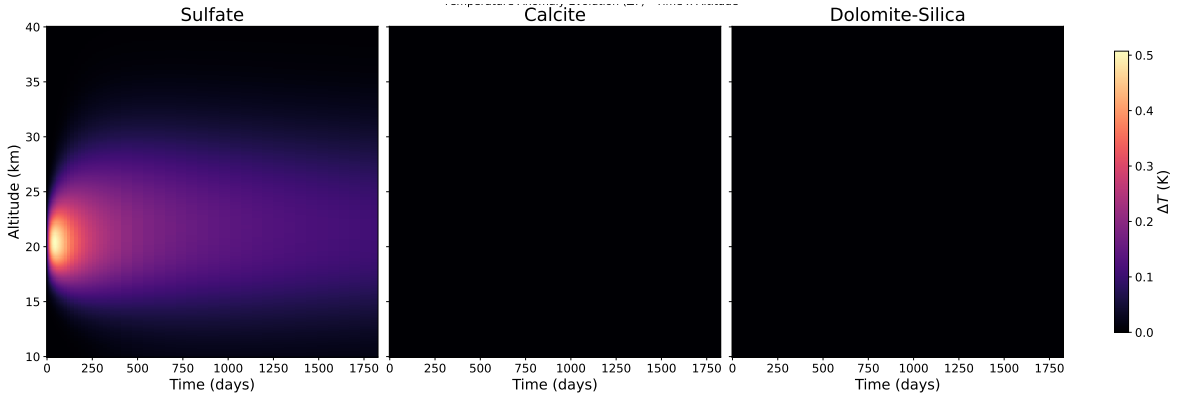

Figure 6. Temperature anomaly $\Delta T(z, t)$ altitude–time heatmaps for all three candidate materials over 1825 days. *Left (Sulfate):* A pronounced warm signal near 20–25 km altitude peaks at day 45 (0.507 K) and decays over the simulation horizon, driven by near-IR absorption at $k \approx 0.027$. *Centre (Calcite)* and *Right (DoloSil-20):* Both mineral panels display no visible temperature anomaly across the entire domain at the color scale shown; ΔT values are at numerical noise floor ($\lesssim 10^{-15}$ K) and are not physically interpretable. This visual contrast constitutes the thermal neutrality criterion of the Trilemma.

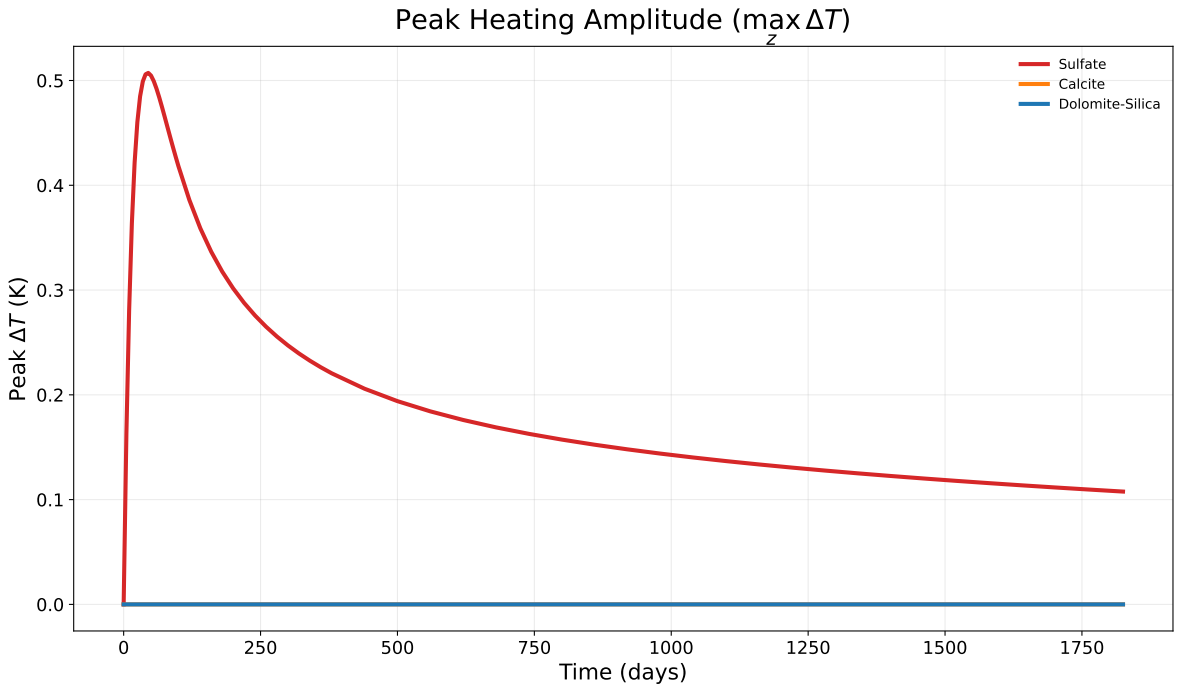

Figure 7. Peak heating amplitude $\max_z \Delta T$ over 1825 days. Sulfate (red) reaches 0.507 K at day 45 then decays to 0.108 K by day 1825. Calcite (orange) and *DoloSil*-20 (blue) lie at the zero baseline at this scale; their values ($\lesssim 10^{-15}$ K) are floating-point noise floor residuals carrying no physical thermal interpretation. The sulfate peak is directionally consistent with prior GCM results [Tilmes et al., 2009] but its absolute magnitude should not be compared to GCM outputs given the 1D column framework.

Table 5. Column mass loading and aerosol optical depth (AOD at 550 nm) at day 0 and day 1825. Mass retention and AOD retention are percentages of the respective day-0 values. Densities drive the settling rate differential via Eq. 6.

Material	ρ_p (kg m^{-3})	M_0 (kg m^{-2})	M_{end} (kg m^{-2})	Mass ret. (%)	AOD$_0$	AOD ret. (%)
Sulfate	1830	3.323×10^{-6}	2.308×10^{-6}	**69.46**	0.00995	**72.24**
Calcite	2710	4.921×10^{-6}	2.645×10^{-6}	53.76	0.01491	56.55
Dolomite core-shell	2850	4.823×10^{-6}	2.603×10^{-6}	53.98	0.01432	56.84

DoloSil-20 core-shell retains 53.98% of its mass (AOD retention 56.84%), approximately 15 percentage points below sulfate at the same time point.

Notably, despite faster sedimentation, the higher per-mass optical efficiency of the core-shell results in a *lower* annual mass replacement rate at equivalent AOD forcing compared to sulfate (Figure 3, centre panel), reflecting that fewer kilograms of the denser, more optically efficient material are needed per unit optical depth. The mass loading decay curves are shown in Figure 8.

4 Discussion

4.1 Physical Interpretation of the Trilemma Resolution

The results demonstrate that within the constraints of this reduced-order 1D screening framework, the three axes of the SAI Trilemma can be simultaneously addressed by material design: a high-n scattering core provides an optical advantage; an absorption-free shell eliminates the thermal penalty; and a size-dependent pore-diffusion barrier limits reactive gas access, suppressing ozone chemistry.

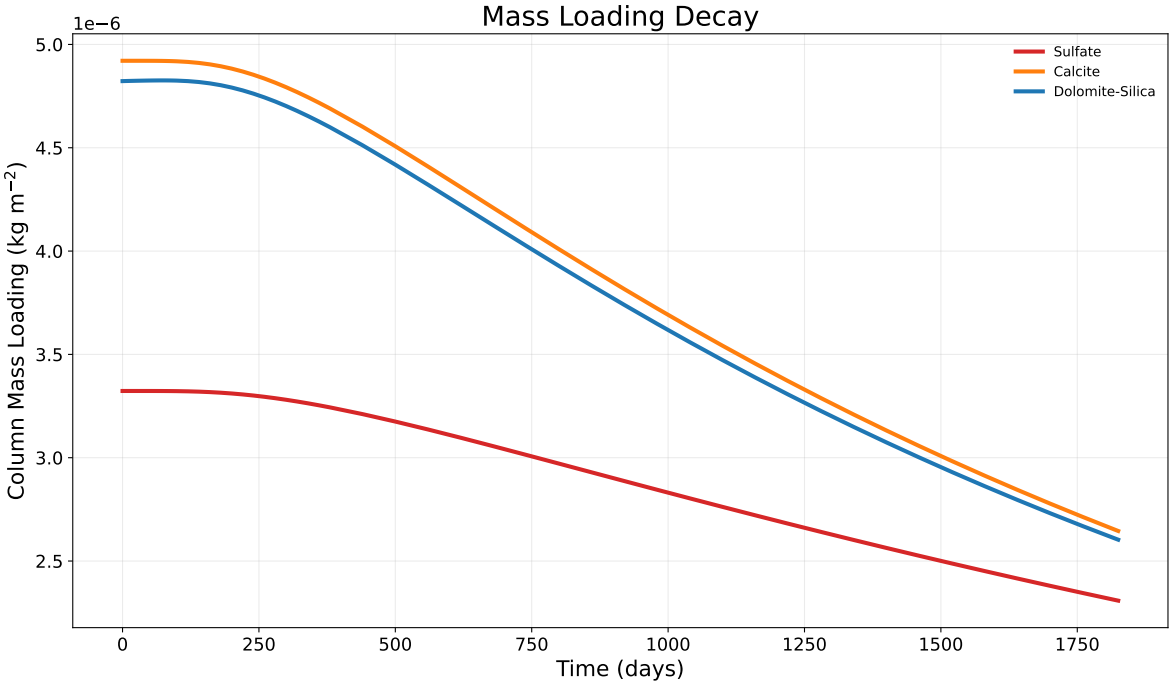

Figure 8. Column mass loading decay over 1825 days for sulfate (red), calcite (orange), and *DoloSil*-20 (blue). Mineral candidates start at higher initial mass loading ($\sim$ 4.8–4.9 $\times$ 10^{-6} kg m^{-2}) owing to their higher densities; sulfate starts at 3.3 $\times$ 10^{-6} kg m^{-2}. At day 1825, mineral candidates retain ~54% of initial mass versus sulfate's 69.46%. The transient negative dM/dt at $t < 50$ days for *DoloSil*-20 reflects coagulation-driven size redistribution during numerical initialization, not actual column mass gain; total column mass is conserved to within solver tolerance throughout.

The +45.17% optical advantage (OPF at the 500 nm design point) arises from two complementary Mie-resonance effects. First, the dolomite core's higher real refractive index ($n = 1.590$) relative to sulfate ($n = 1.430$) increases the refractive index contrast with air, amplifying the Mie resonance strength and thus Q_{sca} (3.8054 vs. 2.6031). Second, the Aden–Kerker core-shell resonance redistributes the angular phase function: the asymmetry parameter g decreases from 0.756 (sulfate) to 0.708 at 500 nm, raising f_{back} from 0.054 to 0.081. These two mechanisms act constructively. The silica shell modifies the effective size parameter and redistributes scattered intensity toward the backward hemisphere via two-interface electromagnetic interference, without introducing absorptive losses.

4.2 Mechanism of Thermal Neutrality

The near-zero ΔT for both mineral aerosols follows directly and mechanistically from the input optical properties: with $k \approx 0$ at 1500 nm (Table 1), there is no imaginary refractive index to drive near-IR absorption. The reported values of 7.09×10^{-16} K and 3.21×10^{-17} K for the *DoloSil*-20 and calcite proxies, respectively, are floating-point residuals; the small difference between them reflects differences in floating-point accumulation paths rather than any physical thermal contrast. This result is *mechanistically expected*: any mineral aerosol with $k_{NIR} \approx 0$ will trivially satisfy the thermal neutrality criterion within this framework. Accordingly, the thermal result is presented as a model consistency check confirming that the model correctly responds to the prescribed optical inputs, not as an independent scientific finding.

Sulfate's finite $k_{NIR} \approx 0.027$ drives the well-documented stratospheric warming signal seen in post-Pinatubo observations [Hansen et al., 1992] and in SAI projections [Tilmes et al., 2009]; the 0.507 K peak anomaly at day 45 in the sulfate proxy is physically meaningful and directionally consistent with prior GCM results, though its absolute magnitude should not be compared to GCM outputs given the 1D column framework.

4.3 Mechanism of Ozone Improvement

The ozone improvement relative to calcite (10.03% vs. 14.77% peak depletion) reflects the additional pore-diffusion barrier provided by the silica shell. Calcite reduces ozone loss primarily through chemical acid buffering: the neutralization of stratospheric H_2SO_4, HCl, and HNO_3 reduces the reactive surface area available for heterogeneous ozone chemistry [Keith et al., 2016]. The *DoloSil*-20 system retains this alkalinity-based buffering while adding the physical diffusion constraint of Eq. (9), which further suppresses the effective reactive uptake coefficient γ_{O_3} from 0.0008 (calcite) to 0.0005 (*DoloSil*-20). This chemical inertness of amorphous silica toward $ClONO_2$ is experimentally supported by Tang et al. [2016], who demonstrated negligible chlorine activation on SiO_2 aerosol surfaces under stratospheric conditions.

The sign of the Pearson correlation coefficient between neutralization flux and ozone column ($r = -0.66$ for *DoloSil*-20; $r = +0.38$ for calcite; Figure S10b of the Supplementary Material) is *consistent with* the expected mechanistic direction, in that higher acid neutralization correlates with less ozone depletion. However, the *DoloSil*-20 data occupy a narrow range of steady-state neutralization flux with only a small number of transient startup points driving the apparent correlation; this limits the statistical inferential power of the r value, and causality between neutralization flux and ozone column is not established within this reduced-order framework.

4.4 The Persistence Trade-off

The principal disadvantage of the *DoloSil*-20 architecture is its reduced atmospheric persistence. The ≈15 percentage-point shortfall in mass retention relative to sulfate at day 1825 is a direct consequence of higher particle density ($\rho_{\text{core}} = 2850\,\text{kg}\,\text{m}^{-3}$ vs. $1830\,\text{kg}\,\text{m}^{-3}$ for sulfate). Via Eq. (6), the Stokes settling velocity scales with $(\rho_p - \rho_{\text{air}})$; the approximately 56% higher effective density of the core-shell aerosol accelerates gravitational sedimentation at all size bins. In a real deployment scenario, this would require a proportionally higher injection rate to maintain equivalent AOD forcing—a logistical consideration rather than a fundamental physical barrier. Since the ozone and thermal safety properties arise from material composition rather than loading level, these advantages are expected to be independent of aerosol burden; however, a formally AOD-normalized comparison was not directly simulated in this study and would require additional runs at adjusted injection loadings.

Additionally, the mass loss rate for mineral aerosols peaks near day 600 before declining, suggesting that a size-distribution biased toward smaller diameters (approaching the settling-only residence-time optimum near $d \approx 300\,\text{nm}$) could potentially improve atmospheric persistence without sacrificing the optical advantage.

4.5 Limitations and Scope of This Study

1. **1D column model, no horizontal transport.** The model is a single idealized vertical column with no horizontal advection, no quasi-biennial oscillation (QBO) coupling, no Brewer–Dobson circulation dynamics, no radiative–dynamical feedbacks, and no tropical-to-polar transport. Three-dimensional GCM simulations are the necessary next step before any deployment-relevant conclusions can be drawn.

2. **Ozone surrogate with unrealistic initialization.** The partial-column DU metric (10–40 km) is a first-order heterogeneous loss surrogate initialized at $\text{DU}_0 = 464.85\,\text{DU}$, which exceeds typical observed 10–40 km partial columns (~250–320 DU; Deshler 2008). Reported depletion percentages are comparative screening metrics only and must not be compared quantitatively to observed or GCM-derived DU anomalies.

3. **Thermal neutrality is a consistency check, not an independent prediction.** The $\Delta T \lesssim 10^{-15}\,\text{K}$ values for mineral proxies are floating-point noise floor residuals. Any material with $k_{\text{NIR}} \approx 0$ will produce this result by construction.

4. **Single-wavelength optical proxy.** β_{back} and the OPF are evaluated at $\lambda = 550\,\text{nm}$ only. Spectrally integrated shortwave radiative forcing requires a full broadband radiative transfer scheme and is beyond the scope of this screening study.

5. **Dolomite birefringence and isotropic approximation.** Dolomite is a negative uniaxial crystal ($n_o = 1.679$, $n_e = 1.500$; Deer et al. 1992), consistent with its negative uniaxial character. The arithmetic-mean isotropic approximation ($n = 1.590$) used here differs from the correct random-orientation average $(2n_o + n_e)/3 \approx 1.619$ by ~1.8%, introducing a comparable systematic uncertainty in Q_{sca}.

6. **Surface uptake parameters require targeted experimental validation.** The intrinsic reactive uptake coefficient $\gamma_{0,\text{base}} = 0.08$ and the pore-diffusion scale parameter r_{scale} are physically motivated estimates. Critically, the *external* reactive interface of the *DoloSil*-20 architecture is the amorphous silica shell, not the dolomite core. The outer-surface chemistry is therefore primarily governed by silica-interface behavior, for which an established literature of surface uptake coefficients and heterogeneous reaction probabilities already exists [Bohren & Huffman,

1983]. This provides partial physical grounding for the assumed surface behavior that does not exist for a fully exposed novel mineral phase. Nevertheless, targeted laboratory flow-tube or Knudsen-cell measurements of γ_0 specifically for the *DoloSil*-20 architecture under stratospheric conditions would further strengthen parameter confidence and quantify any pore-diffusion modification of the bulk silica uptake rate.

7. **Spherical geometry is an idealized upper bound.** The Aden–Kerker solution assumes perfect concentric spheres. Real manufactured core-shell particles exhibit shell-thickness nonuniformity, surface roughness, and core eccentricity that would modify the two-interface electromagnetic interference condition and reduce the backscatter enhancement. The OPF = +45.17% figure should therefore be regarded as an upper-bound estimate for the idealized concentric-sphere geometry.

8. **Hamaker constants and aggregation.** The van der Waals interaction parameters governing *DoloSil*-20 particle aggregation are estimated from silica literature values. AFM colloidal-probe measurements under stratospheric humidity and temperature conditions are recommended before high-confidence aggregation rate modeling.

5 Conclusion

Over a 1825-day reduced-order computational screening simulation, a dolomite core encapsulated by a 20 nm amorphous silica shell simultaneously addresses all three axes of the SAI Trilemma within the constraints of a 1D vertical column framework. At the 500 nm outer diameter design point, the core-shell achieves an OPF of +45.17% in the β_{back} optical screening proxy (0.3405 $\text{m}^2\,\text{g}^{-1}$) relative to the sulfate reference (0.2346 $\text{m}^2\,\text{g}^{-1}$), computed via the Aden–Kerker solution for concentric spheres [Aden & Kerker, 1951, Bohren & Huffman, 1983]; this is a wavelength-specific result at $\lambda = 550$ nm that requires broadband radiative transfer evaluation for conversion to $\text{W}\,\text{m}^{-2}$ forcing, and represents an upper bound for the idealized spherical geometry.

Stratospheric heating is effectively absent for both mineral proxies ($\Delta T \lesssim 10^{-15}$ K), a mechanistically expected consequence of negligible near-IR imaginary refractive index that this framework reproduces as an internal consistency check. Partial-column ozone depletion within the model domain (10–40 km surrogate, not total-column) is suppressed to a screening-level peak of 10.03% compared to sulfate's 47.11%, attributable to the combined chemical acid-buffering of the carbonate core and the physical pore-diffusion barrier of the silica shell—though the latter relies on experimentally unconstrained uptake coefficients. The primary trade-off is an ≈15 percentage-point reduction in 5-year mass retention relative to sulfate (53.98% vs. 69.46%), a direct consequence of higher particle density, partially addressable through injection size-distribution optimization or continuous injection strategies.

These results identify the *DoloSil*-20as a computationally promising SAI screening candidate warranting evaluation in three-dimensional chemistry-climate models. The SAI Trilemma framework and the OPF metric introduced here provide a reproducible multi-criterion basis for comparing candidate materials in future screening studies. Priority validation tasks are: (1) experimental measurement of γ_0 for *DoloSil*-20at stratospheric temperature and pressure via flow-tube or Knudsen-cell techniques; (2) Hamaker-constant characterization via AFM colloidal-probe measurements; (3) T-matrix calculations to assess the effect of dolomite birefringence and quantify the ∼1.8% systematic uncertainty in the isotropic index approximation; and (4) sensitivity analysis of the ozone screening results to the $\gamma_{0,\text{base}}$ and r_{scale} pore-diffusion parameters.

Data Availability

All monthly-averaged simulation output CSV files, optical calculation scripts, and validated metric files are available from the corresponding author upon reasonable request.

Author Contributions

The authors acknowledge the following contributions:

Abdul Haseeb Tanoli (Lead Author): Conceptualization of the SAI Trilemma framework and the Optical Performance Factor (OPF) metric; design and full implementation of the 1D vertical sectional aerosol model (transport, coagulation, sedimentation, heterogeneous chemistry); all optical calculations via Mie theory and the Aden–Kerker analytical coated-sphere solution; analysis and interpretation of all simulation outputs across the 1825-day horizon; synthesis of the trilemma-resolution narrative; identification of the pore-diffusion barrier mechanism and its parametrization; and complete drafting and revision of the manuscript.

Shams ul Arfeen (Co-Author): Critical scientific audit of the screening methodology and computational approach; contributed substantive recommendations that directly shaped the model's design choices, including identification of key physical mechanisms and parameter selection strategies; sustained interdisciplinary knowledge exchange that enabled the convergence of optical, atmospheric, and materials-science reasoning in this work; independent review and analytical scrutiny of key simulation results and their interpretation; and manuscript review, refinement, and assessment of model assumptions, limitations, and scope boundaries.

Acknowledgments

This work is part of the early research output of the **PIEAS Stratospheric Aerosol Injection (SAI) Research Initiative**, a research direction established within the Department of Metallurgy and Materials Engineering at PIEAS. The current study constitutes baseline computational screening work within this broader programme.

The authors thank the open-source developers of PyMieScatt, NumPy, SciPy, and Matplotlib, which were used throughout this work.

The authors acknowledge the use of AI language model systems—including Google Gemini, Anthropic Claude, OpenAI ChatGPT/GPT-4, and DeepSeek—for assistance with critical analysis, discussion refinement, conceptual exploration, and manuscript editing support during the preparation of this work. All scientific content, data, calculations, and conclusions remain the sole responsibility of the authors.

No external funding was received for this research.

Competing Interests

The authors declare no competing interests.

Supplementary Material

Code and Data Availability. The full Python simulation codebase underlying this study—including the 1D sectional aerosol model, Aden–Kerker optical calculations, heterogeneous chemistry routines, and

all post-processing and figure-generation scripts—is not publicly archived at this stage. Researchers interested in accessing the computational code for verification, replication, or collaborative purposes are encouraged to contact the corresponding author directly at bsmme2511@pieas.edu.pk. Requests will be considered on a case-by-case basis.

The following figures are provided as Supplementary Material (S1–S26):

Note on figure organization: Figures S1–S26 in this supplement cover optical screening data, full microphysical evolution, and diagnostic outputs. Primary results (ozone column evolution, ΔT heatmaps, mass loading decay, Aden–Kerker mechanism, and size-resolved AOD) are presented inline in the main text.

S1: Asymmetry parameter g vs. diameter (7 mineral candidates, sphere baseline).
S2: Scattering efficiency Q_{sca} vs. diameter (7 mineral candidates).
S3: Talc settling velocity sensitivity (shape-factor cases AR = 5, 10).
S4: Settling-only residence proxy for talc vs. sulfate over 10 km at 20 km altitude.
S5: Mass(z,t) altitude–time heatmaps for all three candidates.
S6: Surface area density (SAD) evolution (domain mean).
S7: Effective radius (R_{eff}, column-integrated).
S8: Cooling efficiency RF/M (W kg^{-1}, cooling per unit mass).
S9: Mass loss rate $-\mathrm{d}M/\mathrm{d}t$ from column mass loading.
S10: Cumulative mass loss relative to day 0.
S10b: Mechanism check—ozone column vs. H_2SO_4 neutralization flux scatter (Pearson r values; see Section 4.3 for statistical caveats).
S11: Buffering efficiency Φ/A (neutralization per aerosol surface area).
S12: UV/Visible extinction ratio for *DoloSil*-20 (300/550 nm proxy).
S13: Residence time by 5 km altitude bands.
S14: Peak mass concentration altitude vs. time.
S15–S17: 3D size distribution surfaces for sulfate, calcite, and *DoloSil*-20.
S18: Mass-specific aerosol optical depth (AOD/M, m^2 kg^{-1}).
S19: Column particle number loading.
S20: Ozone evolution $O_3(z,t)$ altitude–time heatmaps (all three candidates, showing full spatial depletion pattern).
S21: Neutralization flux (heterogeneous H_2SO_4 uptake proxy).
S22: Radiative forcing proxy (AOD $\times$ -25 W m^{-2}).
S23–S24: Spectral AOD time series (440, 550, 870 nm); Ångström exponent.
S25–S26: Mass-weighted centroid altitude; extinction-weighted centroid altitude.
S27: Altitude of peak ΔT heating. **Note:** For mineral aerosols, this curve tracks the argmax of floating-point noise-floor residuals ($\lesssim 10^{-15}$ K) and carries no physical interpretation; provided for completeness only.

References

Crutzen, P.J., 2006. Albedo Enhancement by Stratospheric Sulfur Injections. *Climatic Change*, **77**(3–4), 211–220.

Rasch, P.J., et al., 2008. An overview of geoengineering of climate using stratospheric sulphate aerosols. *Phil. Trans. R. Soc. A*, **366**(1882), 4007–4037.

Keith, D.W., Weisenstein, D.K., Dykema, J.A., Keutsch, F.N., 2016. Stratospheric solar geoengineering without ozone loss. *Proc. Natl. Acad. Sci. USA*, **113**(52), 14910–14914.

Weisenstein, D.K., Keith, D.W., Dykema, J.A., 2015. Solar geoengineering using solid aerosol in the stratosphere. *Atmos. Chem. Phys.*, **15**(20), 11835–11859.

Deshler, T., 2008. A review of global stratospheric aerosol. *Atmos. Res.*, **90**(2–4), 223–232.

Webster, C.R., et al., 1993. In situ measurements of the ClO/HCl ratio. *Geophys. Res. Lett.*, **20**(22), 2523–2526.

Tilmes, S., et al., 2009. Impact of geoengineered aerosols on the troposphere and stratosphere. *J. Geophys. Res. Atmos.*, **114**, D12305.

Robock, A., et al., 2009. Benefits, risks, and costs of stratospheric geoengineering. *Geophys. Res. Lett.*, **36**, L19703.

English, J.M., Toon, O.B., Mills, M.J., 2012. Microphysical simulations of sulfur burdens from stratospheric sulfur geoengineering. *Atmos. Chem. Phys.*, **12**(10), 4775–4793.

Sumlin, B.J., Heinson, W.R., Chakrabarty, R.K., 2018. Retrieving the aerosol complex refractive index using PyMieScatt. *J. Quant. Spectrosc. Radiat. Transfer*, **205**, 127–134.

Aden, A.L., Kerker, M., 1951. Scattering of Electromagnetic Waves from Two Concentric Spheres. *J. Appl. Phys.*, **22**(10), 1242–1246.

Stöber, W., Fink, A., Bohn, E., 1968. Controlled growth of monodisperse silica spheres. *J. Colloid Interface Sci.*, **26**(1), 62–69.

Ramanathan, V., et al., 2001. Aerosols, Climate, and the Hydrological Cycle. *Science*, **294**(5549), 2119–2124.

Bluth, G.J.S., et al., 1992. Global tracking of the SO_2 clouds from the June, 1991 Mount Pinatubo eruptions. *Geophys. Res. Lett.*, **19**(2), 151–154.

Hansen, J., et al., 1992. Potential climate impact of Mount Pinatubo eruption. *Geophys. Res. Lett.*, **19**(2), 215–218.

Hofmann, D.J., Solomon, S., 1989. Ozone destruction through heterogeneous chemistry. *J. Geophys. Res. Atmos.*, **94**(D4), 5029–5041.

Wilson, J.C., et al., 1993. In Situ Observations of Aerosol and Chlorine Monoxide After the 1991 Eruption of Mount Pinatubo. *Science*, **261**(5125), 1140–1143.

Randel, W.J., et al., 1994. The chemical and radiative effects of the Mount Pinatubo eruption. *J. Geophys. Res. Atmos.*, **99**(D12), 25705–25731.

Bohren, C.F., Huffman, D.R., 1983. *Absorption and Scattering of Light by Small Particles*. Wiley-Interscience, New York.

Dormand, J.R., Prince, P.J., 1980. A family of embedded Runge–Kutta formulae. *J. Comput. Appl. Math.*, **6**(1), 19–26.

Charlson, R.J., et al., 1992. Climate Forcing by Anthropogenic Aerosols. *Science*, **255**(5043), 423–430.

Deer, W.A., Howie, R.A., Zussman, J., 1992. *An Introduction to the Rock-Forming Minerals*, 2nd ed. Longman Scientific & Technical, Harlow, UK.

Robock, A., Marquardt, A., Kravitz, B., Stenchikov, G., 2009. Benefits, risks, and costs of stratospheric geoengineering. *Geophysical Research Letters*, 36, L19703. https://doi.org/10.1029/2009GL039118

Tilmes, S., Müller, R., Salawitch, R., 2008. The sensitivity of polar ozone depletion to proposed geoengineering schemes. *Science*, 320(5880), 1201–1204. https://doi.org/10.1126/science.1153966

Tang, M.J., Keeble, J., Telford, P.J., Pope, F.D., Braesicke, P., Archibald, A.T., Abraham, N.L., McGregor, J., Watson, I.M., Cox, R.A., Pyle, J.A., Kalberer, M., 2016. Heterogeneous reaction of $ClONO_2$ with TiO_2 and SiO_2 aerosol particles: implications for stratospheric particle injection for climate engineering. *Atmos. Chem. Phys.*, **16**, 15397–15412. https://doi.org/10.5194/acp-16-15397-2016

Pope, F.D., Braesicke, P., Grainger, R.G., Kalberer, M., Watson, I.M., Davidson, P.J., Cox, R.A., 2012. Stratospheric aerosol particles and solar-radiation management. *Nature Climate Change*, **2**(10), 713–719. https://doi.org/10.1038/nclimate1528